Quantum Simulations of Interacting Systems with Broken Time-Reversal Symmetry

Yotam Shapira,[1,*,†] Tom Manovitz,[1,*,†,‡] Nitzan Akerman,[1] Ady Stern,[2] and Roee Ozeri[1]
[1]Department of Physics of Complex Systems, Weizmann Institute of Science, Rehovot 7610001, Israel
[2]Department of Condensed Matter Physics, Weizmann Institute of Science, Rehovot 7610001, Israel

(Received 4 July 2022; accepted 4 April 2023; published 9 May 2023)

Many-body systems of quantum interacting particles in which time-reversal symmetry is broken give rise to a variety of rich collective behaviors and are, therefore, a major target of research in modern physics. Quantum simulators can potentially be used to explore and understand such systems, which are often beyond the computational reach of classical simulation. Of these, platforms with universal quantum control can experimentally access a wide range of physical properties. However, simultaneously achieving strong programmable interactions, strong time-reversal symmetry breaking, and high-fidelity quantum control in a scalable manner is challenging. Here, we realize quantum simulations of interacting, time-reversal-broken quantum systems in a universal trapped-ion quantum processor. Using a recently proposed, scalable scheme, we implement time-reversal-breaking synthetic gauge fields, shown for the first time in a trapped-ion chain, along with unique coupling geometries, potentially extendable to simulation of multidimensional systems. Our high-fidelity single-site resolution in control and measurement, along with highly programmable interactions, allow us to perform full state tomography of a ground state showcasing persistent current and to observe dynamics of a time-reversal-broken system with nontrivial interactions. Our results open a path toward simulation of time-reversal-broken many-body systems with a wide range of features and coupling geometries.

DOI: 10.1103/PhysRevX.13.021021

Subject Areas: Atomic and Molecular Physics, Quantum Physics

I. INTRODUCTION

Quantum many-body systems are abundant in nature and lie at the heart of contemporary physical research. These systems exhibit complex collective behavior and interesting phases which emerge due to interactions between the systems' constituents. Often, richer phenomena are observed when placing such systems in the presence of time-reversal symmetry-breaking (TRSB) fields, such as magnetic fields. A stark example is the appearance of anyonic excitations in the fractional quantum Hall effect [1–5].

Typically, quantum many-body systems are analytically intractable and are not amenable to numerical simulation techniques beyond small sizes. Thus, in the past three decades, tremendous effort has been put forth to develop and employ quantum simulation in order to study such systems [6,7]. Of the variety of physical platforms used for simulating quantum systems with TRSB, ultracold gases of neutral atoms have emerged as particularly prolific [8]. Here, TRSB magnetic fields can be generated by a variety of techniques, including rotation of the gas, optical dressing, or Floquet engineering [8,9], and have been utilized to great effect in various experiments [9–20]. Recently, programmable couplings have also been realized in ultracold gasses trapped in an intracavity optical lattice [21].

TRSB quantum simulation has also been realized in other platforms, including qubit systems. Some of these platforms can also serve as fully programmable, universal quantum computers. Progress in such platforms has culminated in TRSB demonstrations with superconducting circuits [22,23] and neutral atoms held in optical tweezers 24]]. Despite the restricted Hilbert spaces, qubit platforms with TRSB can support a variety of exotic phases such as spin liquids and fractional quantum Hall states [25,26] and can make use of a powerful quantum control tool set, potentially enabling state tomography; energy spectrum measurement [23]; measurement of topological string operators [27]; quantum-classical variational optimization [28]; the use of randomized measurements to estimate a range of complex observables [29,30]; and the measurement of entanglement entropy through swap tests [31].

Trapped-ion chains are one of the leading technologies for both quantum simulation [6] and quantum information

*These authors contributed equally to this work.
†Corresponding author.
‡Present address: Department of Physics, Harvard University, Cambridge, Massachusetts 02138, USA.

processing (QIP) [32–34], due to unparalleled quantum control fidelity and measurement accuracy. In a typical trapped-ion-chain platform, an array of ions is confined to a one-dimensional chain in a linear Paul trap, and a qubit is encoded on each ion by isolating two energy levels. Qubits can then be coupled by mediating interaction through the motional modes of the ion chain [35]. A unique advantage of trapped-ion platforms for both quantum simulation and QIP is their natural long-range connectivity, itself a product of the long-range Coulomb interaction mediating the coupling of ions. These properties are used in an assortment of state-of-the-art quantum simulations [36–40].

Here, we realize an analog quantum simulator of TRSB systems in a small trapped-ion quantum processor [41]. We use a recently proposed method [42], in which experimentally simple additions to the typical ion QIP tool set provide scalable access to highly programmable interactions, including TRSB synthetic fields and emergent coupling geometries that significantly differ from the one-dimensional physical geometry of the ion chain. Using these flexible tools, as well as the quantum control afforded by our quantum processor, we generate a ground state of an interacting Aharonov-Bohm (AB) ring, which we investigate using state tomography and via ground-state certification [43]; we observe the gauge-field-dependent dynamics of the ring model.

Furthermore, we explore the dynamics of a TRSB triangular ladder system. This model may be scaled to simulate two-dimensional systems using the one-dimensional chain. The triangular ladder possesses a wide set of symmetries, including the $C_2\mathcal{T}$, which generates a nontrivial spin-current structure. This symmetry occurs in several condensed matter systems where it has significant consequences on the electronic band structure and topological properties [44,45]. Moreover, the two-dimensionality of the triangular model leads to the appearance of interactions between quasiparticles, in which an excitation hops between next-nearest-neighbor sites, conditioned on the occupation of the intermediate site. Our results are the first realization of TRSB in a trapped-ion-chain quantum simulator with programmable interactions and delineate a path toward realizing highly flexible and multidimensional coupling geometries in these systems.

We review previous experimental results in the vein of those presented here, highlighting similarities and differences. Triangular TRSB models have been realized in superconducting circuits in Refs. [22,46] and in Rydberg atoms in Ref. [24]. All of these experiments mark a significant advance in analog quantum simulations.

Specifically, in Ref. [24], a triangular model is constructed from three Rydberg atoms. The implemented Hamiltonian is identical to our own when limited to the single-excitation subspace, leading to similar dynamics. However, in contrast with the results shown here, time-reversal symmetry is no longer broken in the two-excitation subspace.

In Ref. [22], the authors similarly generate a triangular AB ring and explore its dynamics when initialized with one excitation and two excitations. In the latter, interactions allow the dynamics to be mapped onto a counterpropagating single-excitation hole. That is, although the model is interacting, it can be easily interpreted as a free-fermion model. However, our realization of a four-site triangular ladder constitutes the smallest nontrivial geometry in which the role of interactions cannot be mapped to physics of single particles. Specifically, the dynamics we observe in the two-excitation subspace does not resemble freely evolving fermions.

In Ref. [46], the authors generate models with up to five spin sites but restrict their system to the single-excitation subspace, such that excitation-excitation interactions do not play a role in the observed dynamics.

Last, we remark that there is a tremendous synergistic effect to the parallel research that is carried out on different physical platforms, with each platform bringing its own strengths and limitations. Trapped-ion systems, for example, allow for connectivity between qubits that are not nearest neighbors and to distances much larger than those allowed by other platforms in an analog setting. Indeed, our experiment makes use of this connectivity, which allows us to position ions on a one-dimensional line yet construct a system that has a larger dimension spin connectivity with programmable complex-valued couplings. As we show in Ref. [42], the techniques demonstrated here are directly extendable to simulation of much more complex coupling geometries.

Our method enables simulation of a variety of models that can be described through the general spin Hamiltonian:

$$H = \sum_{n=1}^{N-1} H_n = \sum_{n=1}^{N-1} \Omega_n e^{i(\phi_n - \delta_n t)} \sum_{k=1}^{N-n} \sigma_{k+n}^{+} \sigma_k^{-} + \text{H.c.}, \qquad (1)$$

where σ_k^+ (σ_k^-) denotes a spin-raising (-lowering) Pauli operator on site k out of N and Ω_n, ϕ_n, and δ_n are experimentally tunable parameters that, respectively, correspond to the coupling strengths, static phases, and time-dependent phases of an n-neighbor-hopping interaction.

The theoretical proposal underpinning our work and derivation details of Eq. (1) are provided in Ref. [41]. Here, we review the physical picture and main components required for its realization. Our method consists of three conceptual steps: We generate $\sigma^+\sigma^-$ couplings between all ion pairs in the chain, then sever all of these couplings, and, finally, selectively reinstate the couplings which are relevant to the simulated model.

The first step is achieved by driving red and blue sidebands of the center-of-mass normal mode of motion of the ion chain. This couples the ions' internal, i.e., qubit, states to the motional state of the chain and typically generates a spin-dependent force. By sufficiently detuning

our drive from the sidebands, we adiabatically eliminate them and generate effective $\sigma^+\sigma^-$ spin-hopping couplings acting only on the qubit degrees of freedom. Since this interaction is mediated through the center-of-mass mode, which equally involves all ions, then all ion pairs are equally coupled. Next, we sever these all-to-all couplings by introducing a magnetic field gradient along the ion-chain axis, such that the qubit transition frequency difference between adjacent ions, Δ, is larger than the rate of the $\sigma^+\sigma^-$ couplings, making it nonresonant. Last, we reinstate specific H_n terms by modulating the sideband drive. Specifically, for each desired H_n term, we modify our drive and generate a pair of spectral tones which couple to the sideband and have a frequency difference of $n\Delta$ that bridges the energy gap opened between ions that are n sites apart, making the $\sigma_k^+\sigma_{k+n}^-$ process resonant. We note that time-reversal symmetry is explicitly broken by the magnetic field gradient, as a hop in one direction of the ion chain is energetically different than in the other. This is utilized by setting the phase difference between the two tone pairs, which generates the phase ϕ_n.

We encode qubit states, $|0\rangle$ and $|1\rangle$, on the $|5S_{1/2}, m=\frac{1}{2}\rangle$ and $|4D_{5/2}, m=\frac{3}{2}\rangle$ orbitals, respectively, of $^{88}Sr^+$ ions held in a linear Paul trap. These state are coherently coupled using a narrow-linewidth 674-nm laser [47]. We utilize our 674-nm laser in a global path, homogeneously illuminating all ions, and in an individual path, in which a tightly focused beam can address a single ion at a time and light shift its qubit transition. The multitone modulation of the laser drive required for our implementation is generated by driving an acousto-optic modulator controlling the global 674-nm path using an arbitrary waveform generator, resulting in effective couplings, Ω_n, of a few hundreds of hertz. The magnetic field gradient is realized along the ion-chain axis, generating an approximately 1-kHz frequency difference between neighboring ions. Our implementation is amenable to scaling up, as the addition of more sites to the models requires only slight modifications to the spectral components driving the interaction [42].

The simple form in Eq. (1) encodes a rich family of spin models in various dimensions and geometries. Figure 1(a) shows a linear chain of ions and couplings utilizing nearest-neighbor (NN), next-nearest-neighbor (NNN), and periodic boundary conditions with respective coupling strengths Ω_1, Ω_2, and Ω_{N-1}. The specific models implemented here are also shown: a three-ion AB ring (b) threaded by a flux Φ_{AB} and a triangular spin ladder (c) threaded by a staggered flux Φ_S.

The spin Hamiltonian (1) can be mapped to a hard-core boson model by identifying a spin excitation with a bosonic excitation ($\sigma^+ \leftrightarrow b^\dagger$) or to a fermionic Hamiltonian through one of several mappings. Indeed, using a Jordan-Wigner transformation [48], the Hamiltonian in Eq. (1) is rewritten as

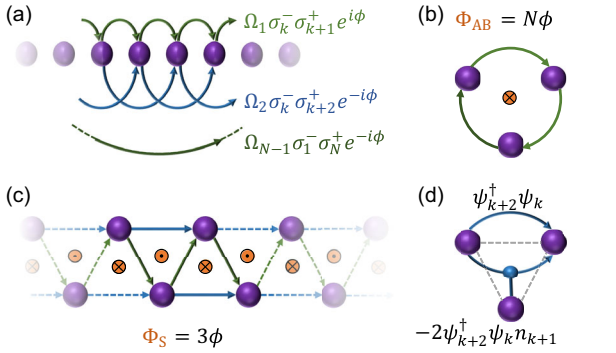

FIG. 1. Mapping of an ion chain to spin models. (a) A linear chain of ions is coupled with NN hopping (light green), NNN hopping (blue), and periodic boundary condition hopping (dark green). Each of these interactions is accompanied by a tunable phase, ϕ. (b) Setting $\Omega_1 = \Omega_{N-1} = \Omega$ (and all others to zero) forms an N-site AB ring, penetrated by a flux $\Phi_{AB} = N\phi$ (orange). (c) Instead, setting $\Omega_1 = \Omega_2 = \Omega$ (and all others to zero) forms a triangular ladder. Each plaquette of the ladder is penetrated by a staggered flux, $\Phi_S = 3\phi$ (orange). (d) Transforming to a fermionic Hamiltonian reveals that the triangular ladder is an interacting model. Indeed, a hop along the ladder's rails is possible through two terms, a two-body trivial term and an interacting four-body term for which the hop from site k to $k+2$ is conditioned on the occupation of site $k+1$.

$$H = \sum_{n=1}^{N-1} \Omega_n e^{i(\phi_n - \delta_n t)} \sum_{i=1}^{N-n} \psi_{i+n}^\dagger \psi_i e^{i\pi \sum_{k=i+1}^{i+n} n_k} + \text{H.c.}, \quad (2)$$

where ψ_i denotes a fermionic annihilation operator at site i and $n_k = \psi_k^\dagger\psi_k$ is the occupation at site k. Using this Hamiltonian form for the triangular spin ladder reveals that the model is interacting, as hopping operators along the ladder's rails are composed of two-body hop terms and four-body correlated hop terms, shown in Fig. 1(d).

We note that the spin Hamiltonian (1) commutes with the total spin (excitation) operator $\sum_{k=1}^N \sigma_k^z$—i.e., the dynamics preserves the total spin—and can, therefore, be decomposed to total spin-excitation subspaces. We utilize this by initializing our system in either the single-excitation subspace (1ES) or the two-excitation subspace (2ES), which are free of dephasing due to global phase noise. This allows us to observe coherent dynamics for times exceeding our single-qubit coherence time by an order of magnitude [49].

II. TIME-REVERSAL SYMMETRY BREAKING IN THE AHARONOV-BOHM RING

The AB ring consists of N sites placed on a ring, with NN hopping allowed, and threaded by a magnetic flux Φ. Because of the AB effect, the system exhibits persistent currents, which survive even in the presence of impurities [50,51]. We realize an $N = 3$ AB ring and investigate the dynamics of one and two excitations on it. We also adiabatically prepare the ring's ground state in the singly

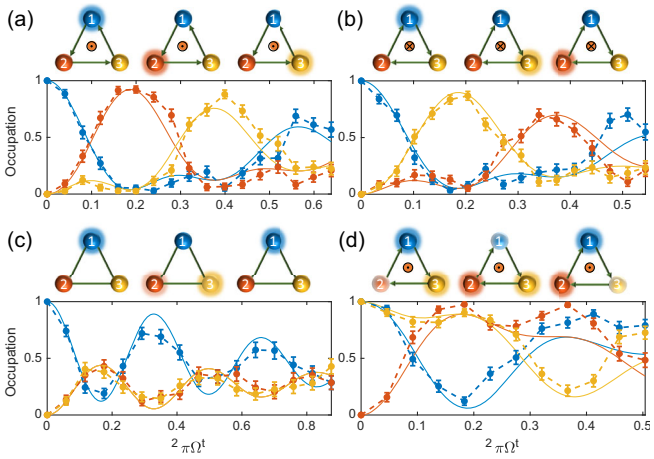

FIG. 2. Dynamics in the AB ring, exhibiting TRSB patterns. Schematic (top of each subplot) shows flux direction (orange) and observed spin currents (green arrows). Site colors and numbering correspond to the data (bottom of each subplot). Site occupation data (point and dashed lines) are postselected to the relevant excitation subspace and compared to theoretical prediction which includes dephasing estimations (solid lines), showing a good fit. Error bars represent 2σ regions due to quantum shot noise (see Appendix C). (a) Initialization to site 1, with flux $\Phi_{AB} = \pi/2$. The excitation "hops" in a counterclockwise manner around the ring to site 2 and then 3, following the spin-current arrows. (b) Similarly, by initializing to the same state with $\Phi_{AB} = -\pi/2$, the evolution becomes clockwise. (c) For $\Phi_{AB} = 0$, time-reversal symmetry is restored and the system does not have a preferred direction of rotation; hence, the excitation "splits" equally clockwise and counterclockwise and recombines at site 1. (d) Initialization to sites 1 and 2, in the 2ES, with $\Phi = \pi/2$. The system can be mapped to a noninteracting hole (light colors) initialized at site 2.

excited manifold. While the AB ring is an analytically solvable model that has been subject to extensive research [22,24,46,52–56], it is useful for demonstrating a broken time-reversal symmetry and instructive as a validation of our method.

The AB ring Hamiltonian is given by

$$H_{AB}(\Phi) = \Omega \sum_{n=1}^{N} \sigma_{i+1}^{+} \sigma_i^{-} e^{i\Phi/N} + \text{H.c.}, \tag{3}$$

with $N + 1 \equiv 1$ and Ω an effective coupling between the ring's sites.

An apparent manifestation of the persistent currents in this model is transport of excitations around the ring. This is demonstrated by quenching an excitation on an $N = 3$ AB ring to specific sites and observing the site occupation at different evolution times. Figure 2 shows several examples of these dynamics. In our experimental setup, we measure independently the state of each ion, which we use in order to postselect and normalize our results to the relevant subspace; e.g., when initializing a single excitation, we normalize $\Pr(|100\rangle) \mapsto \Pr(|100\rangle)/[\Pr(|100\rangle) + \Pr(|010\rangle) + \Pr(|001\rangle)]$ (see Appendixes A and B). We compare the dynamics to a numerical evaluation of the evolution, with Ω obtained by a maximum likelihood (ML) fit.

Figure 2(a) shows the evolution of an excitation on site 1, i.e., the state $|100\rangle$, with $\Phi_{AB} = \pi/2$. Here, the excitation traverses the ring sites in a counterclockwise manner, i.e., $1 \to 2 \to 3 \to 1$. A single excitation in the three-site AB ring is, to a high degree of accuracy, a wave packet; hence, the excitation does not disperse for long evolution times. Moreover, for $\Phi_{AB} = \pm\pi/2$, the evolution is periodic. (b) Using the opposite flux, $\Phi_{AB} = -\pi/2$, the evolution becomes clockwise, i.e., $1 \to 3 \to 2 \to 1$. Setting the flux to $\Phi_{AB} = 0$ (c), time-reversal symmetry is restored and the excitation equally occupies sites 2 and 3, before recombining back at site 1.

Furthermore, we initialize the system to sites 1 and 2 in the 2ES with $\Phi_{AB} = \pi/2$, shown in Fig. 2(d). While the two excitations are interacting, their resulting dynamics may be transformed to a noninteracting "hole" occupying site 3 [22], which rotates around the ring in the opposite direction to that of an excitation. That is, the dynamics in the 2ES are readily mapped to a free-fermion model. As we show below, this is not the case in the interacting triangular ladder.

The population evolution shown in Fig. 2 clearly exhibits dephasing, which does not exist in the AB model. The dephasing is generated by the small occupation of states outside of the decoherence-free subspace (DFS), which are used to mediate the interaction between the ring's site. The extent of the dephasing is estimated and added to the theoretical prediction (solid lines) with no additional fitting parameters (see Appendixes A and B). Furthermore, our analysis shows that, by increasing the system's single-qubit coherence time or the drive power, dephasing can be largely mitigated and does not constitute a hurdle in scaling up the simulation size.

Next, we investigate the ground state in the single-excitation subspace of the AB ring. In order to optimally utilize our coherence time, we slightly deviate from the adiabatic regime prescribed by Ref. [42]. This acts to add small unwanted nonresonant terms to the Hamiltonian, such as $\sigma^{+}\sigma^{-}$ terms with no complex phase, i.e., $\Phi_{AB} = 0$ terms. Thus, in our ground-state preparation below, we generate the modified Hamiltonian $H_{\text{eff}} = H_{AB}(\Phi_{AB}) + \epsilon H_{AB}(0)$. We extract ϵ from our data below using a fit, obtaining $\epsilon = 0.22$ (see Appendix D).

We prepare the ground state of H_{eff} using the following steps. We initialize the system in the state $|100\rangle$ in the 1ES. We then turn on the Hamiltonian $H_0 = -\delta\sigma_1^z$, which lowers the energy of this state, making it the ground state of H_0 in the 1ES. Last, we adiabatically ramp down H_0 and ramp up H_{eff}. Specifically, the ramp is implemented by the Hamiltonian

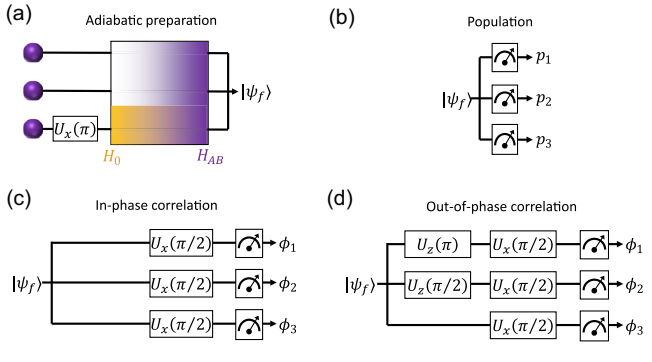

FIG. 3. Adiabatic preparation protocol of the AB ring ground state. (a) Adiabatic preparation. We initialize the state $|001\rangle$ by rotating a single site with $U_x(\pi)$, lower the site's energy with H_0 (orange), and slowly ramp H_0 down while ramping H_{eff} up (purple). The ground state is ideally reached at the end of the ramp. (b)–(d) We perform tomography of the resulting state by measuring site occupation (b), in-phase correlations via U_x pulses (c), and out-of-phase correlations via additional U_z rotations (d).

$$H(t) = [1 - (t/T)^2]H_0 + (t/T)^2 H_{\text{eff}}, \tag{4}$$

where T is a long ramp time. When adiabaticity holds, we expect the resulting state $|\psi_f\rangle$ to be the ground state of the AB ring in the 1ES. When the gap between the ground state and the next excited level is small, specifically, for $|\hbar^2\delta/T(\Delta E)^2| \gg 1$, with ΔE the gap between the ground state and the next excited level, Landau-Zener transitions cause a breakdown of adiabaticity.

Utilizing the fact that our quantum simulator is embedded in a universal quantum processor, we perform tomography of the resulting state $|\psi_f\rangle$. This requires three independent measurements of $|\psi_f\rangle$: occupancy of the ring's sites; in-phase correlations between the sites, obtained by operating with an additional global x spin rotation, $\prod_n U_n^x(\pi/2)$, prior to the measurement; and out-of-phase correlations, obtained by performing an additional, $U_2^z(\pi/2)U_3^z(\pi)$ rotation, prior to the global x rotation. For a general pure state in the 1ES, $|\psi\rangle = \sqrt{p_1}e^{i\phi_1}|100\rangle + \sqrt{p_2}e^{i\phi_2}|010\rangle + \sqrt{p_3}e^{i\phi_3}|001\rangle$, the occupancy measurement yields the p_n's, and the correlation measurements yield the ϕ_n's (up to a global phase), which allows us to assess the preparation process in full. Figure 3 schematically shows the adiabatic preparation [Fig. 3(a)] and measurement sequences [Figs. 3(b)–3(d)]. We remark that our results use postselection in the 1ES and assume rapid dephasing of coherences between and in other excitation subspaces.

We use the tomographic measurements in order to directly assess the ground-state preparation fidelity. However, such a method clearly becomes infeasible for larger ion chains. We, therefore, compare these results to a direct certification protocol, based on the method in Ref. [43]. This method uses exclusively energy measurement of the prepared state, which scales linearly with the system size, and not the full tomographic data. Here, we use the tomographic data to compute the state energy and compare our fidelity estimates to the certification's results in order to benchmark its performance.

This certification tests ground-state preparation of Hamiltonians which are composed of local interactions [e.g., the Hamiltonian in Eq. (1)] and have a known ground-state energy and known gap to the next excited state. Ideally, certification would imply that candidate ground states with a fidelity, i.e., overlap with the ground state, $F = |\langle\psi|\psi_{\text{GS}}\rangle|^2$, which is below a predetermined threshold F_T, will be "rejected" and above the threshold will be "accepted." Here, because of the use of only energy measurements, with finite accuracy, the criterion is slightly weakened. For a state with fidelity $F < F_T$ the protocol rejects the state with probability $1-\alpha$, where α, the "reliability," depends on the simulated model and measurement parameters and is ideally small. Furthermore, the complementary case is also slightly weakened. That is, states with fidelity $F > F_T + \delta$ are also accepted with probability $1-\alpha$; however, no guarantee is given for states with fidelity $F_T < F < F_T + \delta$, where δ is an ideally small, yet nonzero fidelity gap, which also depends on the simulated model and measurement parameters. The certification operates by converting the fidelity threshold F_T to an upper energy bound E_T, which is compared to the measured energy and satisfies the reliability described above. Here, we choose the threshold $F_T = 0.7$, as it corresponds to the average expected fidelity of our preparation protocol.

We repeat this process for various values of flux Φ_{AB} and evaluate the prepared state. Our results are shown in Figs. 4(a)–4(d). The spectrum of H_{eff} as a function of Φ is shown in Fig. 4(a). Energies are normalized by a characteristic coupling scale $\Omega = 350$ Hz. For $\Phi_{\text{AB}} = 0$, the ground state (dashed blue line) is well separated from the other states; however, at $\Phi_{\text{AB}} = \pm\pi$, the spectral gap is small. Accordingly, the gray region (here and in all other subplots) marks fluxes where Landau-Zener transitions limit our ground-state preparation fidelity. Nevertheless, the prepared state's energy (solid blue line), computed using the tomographic measurements, fits very well to the ground-state energy. Here (and in all other subplots), error bars mark 2σ errors due to quantum projection noise.

The green region marks energy values for which state certification [43] accepts the prepared ground state. Figure 4(b) shows accordingly which states are accepted (green) and rejected (red) and the certification's reliability α. Clearly, when the ground-state energy gap is sufficiently large, the prepared states are accepted within a reasonable success rate.

Figure 4(c) shows the overlap of the prepared states based on the tomographic measurements (solid line), with $|S_{1,2,3}\rangle$, the three eigenstates of H_{eff}, with $|S_1\rangle$ the ground state. The measurements are compared to an estimation (dashed line) based on a simulation (see Appendix D). We

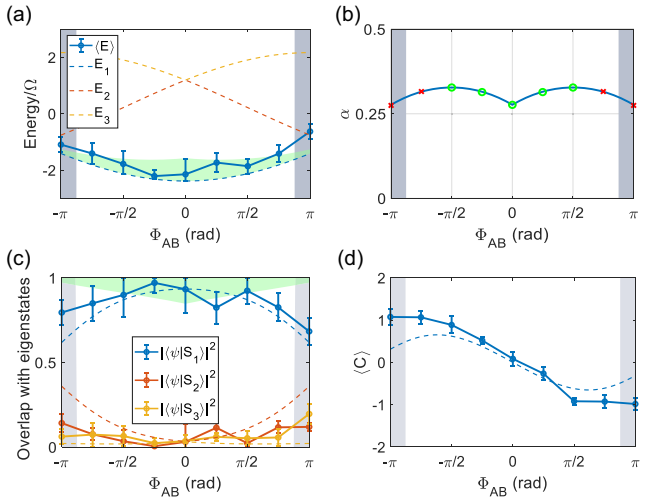

FIG. 4. Evaluation of the AB ring ground state. Error bars represent 2σ regions due to quantum shot noise. (a) Spectrum of H_{eff} (dashed lines) and measured energy of the prepared states (solid lines), showing good agreement. The spectral gap from the ground state is small at $\Phi_{\mathrm{AB}} = \pm\pi$, leading to a breakdown of adiabaticity, marked by the gray region. "Accept" energy values for ground-state certification are marked in the green region, i.e., values for which $E < E_T$. (b) Accepted (green) and rejected (red) states and the corresponding reliability α. (c) Overlap of prepared state with the eigenstates $|S_{1,2,3}\rangle$ of H_{eff}. The ground state $|S_1\rangle$ is accurately prepared in the adiabatic region, with a peak overlap of $0.97^{+0.03}_{-0.05}$. The preparation degrades in the nonadiabatic region. The green region marks the certification fidelity $F_T + \delta$, for which states are accepted with probability $1 - \alpha$. We note that this region has a good overlap with the fidelity estimation of accepted states. (d) Expectation value of the current operator. The ground state exhibits a persistent nonvanishing current that changes sign around $\Phi_{\mathrm{AB}} = 0$. The measured value (solid line) is in good agreement with the theoretical expectation (dashed line).

observe good agreement between measurement and expectation, with a peak overlap with the ground state of $0.97^{+0.03}_{-0.05}$. We further notice that this overlap degrades in the nonadiabatic (gray) regions as expected. The green region marks the fidelity region $F > F_T + \delta$ of accepted certified states, in correspondence to Fig. 4(a). We note that this region varies with Φ_{AB}, as δ depends on the ground-state energy gap [43]. We comment that the occupation of the different sites of the prepared ground states is long lived and dictated by the single-qubit lifetime, which is longer than the evolution times used here. However, similarly to the dynamics shown above, the coherence between these populations decays.

Finally, our prepared ground states exhibit nonvanishing persistent spin currents, which mark the broken time-reversal symmetry generated by the AB flux. We compute the expectation value of the spin-current operator, $C = i\sum_{n=1}^{N}(\sigma_{n+1}^{+}\sigma_n^{-}e^{i\Phi_{\mathrm{AB}}/N} - \mathrm{H.c.})$, using the tomographic measurements. As shown in Fig. 4(d), this expectation value varies between positive and negative values according to Φ_{AB}, demonstrating good agreement between the theoretical prediction (dashed line) and measured (solid line) values of spin currents in the ground state.

III. INTERACTIONS ON A TRIANGULAR LADDER

While the one-dimensional Aharonov-Bohm ring is convenient for clearly illustrating TRSB and periodic boundary conditions, it is an exactly solvable free-fermion model and, thus, is not an interesting target for future quantum simulation. However, by slightly varying the coupling geometry, it is easy to generate models with TRSB which cannot be reduced to free fermions and which inherently include interactions.

Specifically, we set $\Omega_1 = \Omega_2 = \Omega$ (and null all other couplings) in the spin Hamiltonian in Eq. (1) and form triangular plaquettes that make up the ladder coupling configuration shown in Fig. 1(c). The ladder's rungs (diagonal green lines) are formed by the NN term and its rails (horizontal blue lines) are formed by the NNN terms. We set $\phi_1 = -\phi_2$, thereby generating a staggered flux of $\Phi_S = 3\phi$ through the plaquettes. Although the total flux nulls, time-reversal symmetry is still broken by the local gauge invariant flux.

Here, we focus on $\Omega_1 = \Omega_2 = \Omega$; however, Ω_1 and Ω_2 can be fully controlled using our technique, and different coupling strength ratios can generate interesting models which can support a variety of phases, including ordered dimerized, Luttinger liquid, and chiral-ordered phases [29,57–67].

The model's Hamiltonian in its fermionic form is

$$H_{\mathrm{tl}} = \Omega\sum_k(\psi_{k+1}^{\dagger}\psi_k + \psi_k^{\dagger}\psi_{k+2}[1-2n_{k+1}])e^{i\phi} + \mathrm{H.c.}, \quad (5)$$

which is an interacting Hamiltonian. Indeed, the term $\psi_k^{\dagger}\psi_{k+2}$ has a single-particle contribution but also an interacting four-body term, which conditions the NNN hop on the occupation of the intermediate site, as depicted in Fig. 1(d).

We make use of a gauge transformation and analyze the model in its spin form:

$$H_{\mathrm{tl}} = \Omega\Big(\sum_{k\ \mathrm{odd}}\sigma_{k+1}^{+}\sigma_k^{-} + \sum_{k\ \mathrm{even}}e^{i\Phi_S}\sigma_{k+1}^{+}\sigma_k^{-} + \sum_k\sigma_k^{+}\sigma_{k+2}^{-}\Big) + \mathrm{H.c.} \quad (6)$$

The gauge choice in Eq. (6) makes the model's symmetries apparent, which is helpful in its analysis (see Appendix E). Namely, for a $N = 4$ minimal triangular ladder, we observe a unitary symmetry, $U_{1,4} = (1 + \sigma_1^x\sigma_4^x + \sigma_1^y\sigma_4^y + \sigma_1^z\sigma_4^z)/2$, which swaps sites 1 and 4, and an antiunitary symmetry $A = U_{2,3}K$, with K the complex conjugation operator. Furthermore, the staggered flux $\Phi_S = \pm\pi/2$ gives rise to an additional chiral symmetry

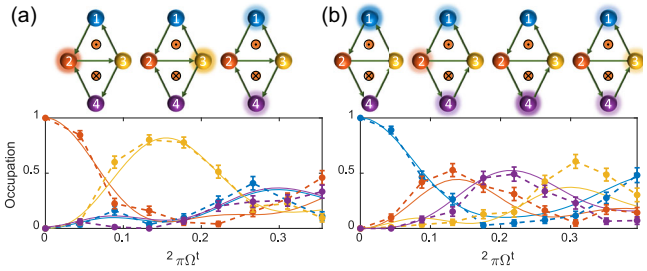

FIG. 5. Dynamics on a triangular ladder in the 1ES with $\Phi_S = \pi/2$, exhibiting TRSB patterns. Schematic (top) shows staggered flux direction (orange) and observed spin currents (green arrows). Site colors and numbering correspond to the data (bottom). Site occupation data (point and dashed lines) are postselected to the 1ES and compared to theoretical prediction which includes dephasing estimations (solid lines), showing a good fit. Error bars represent 2σ regions due to quantum projection noise. (a) Initialization at $|2\rangle$. The evolution follows the green spin-current arrows; i.e., the state hops to site 3, then splits to sites 1 and 4, and finally recombines at 2. For clarity, the theoretical blue curve for site 1 is slightly shifted. (b) Initialization to $|1\rangle$. The peak population encompasses the ladder in a counterclockwise manner.

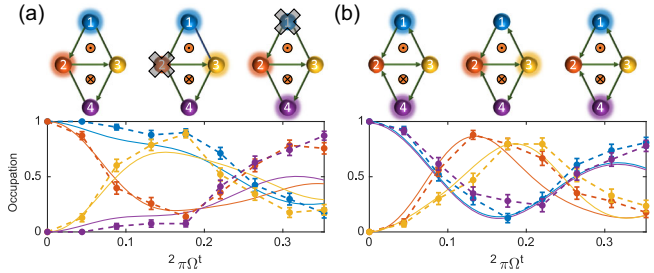

FIG. 6. Dynamics on a triangular ladder in the 2ES with $\Phi_S = \pi/2$, exhibiting interactions. Schematic (top) shows staggered flux direction (orange) and observed spin currents (green arrows). Site colors and numbering correspond to the data (bottom). Site occupation data (point and dashed lines) are postselected to the 2ES and compared to theoretical prediction which includes dephasing estimations (solid lines), showing a good fit. Error bars represent 2σ regions due to quantum shot noise. (a) Initialization in $|1,2\rangle$. Evolution is affected by the four-body interaction term, resulting in a hop to $|1,3\rangle$, as opposed to the 1ES evolution $1 \to 2$ (represented by a cross over site 2). The next hop similarly is to $|2,4\rangle$, which does not follow the 1ES evolution of $3 \to 1$. (b) Initialization to $|1,4\rangle$. The system exhibits oscillations with period $T_{2\mathrm{ES}}/3$. For clarity, the theoretical curve for site 4 is slightly shifted.

$C = \sigma_1^z \sigma_4^z U_{2,3}$, which anticommutes with the Hamiltonian. An analogous fermionic representation can be constructed by the Jordan-Wigner transformation.

We first focus on the 1ES. Because of $U_{1,4}$, the state $|S_1\rangle \equiv |S\rangle_{1,4}|00\rangle_{2,3}$, with $|S\rangle_{i,j}$ a singlet of sites i and j, is decoupled from the rest of the spectrum and carries zero energy. Because of the existence of the chiral antisymmetry C, the remaining three states in the 1ES have energies $\pm E_1$ and 0, where E_1 is computed by diagonalization, yielding $E_1 = \sqrt{5}\Omega$. Thus, the 1ES spectrum is equally spaced, leading to a periodic evolution with period $T_{1\mathrm{ES}} = 2\pi/\sqrt{5}\Omega$. We quench the system by initializing a single local excitation.

We initialize the system to $|2\rangle = \sigma_2^+|0000\rangle$ in the 1ES and observe the system's dynamics. This state is an eigenstate of $U_{1,4}$ with an eigenvalue of $+1$; thus, this symmetry is preserved throughout the evolution. Indeed, Fig. 5(a) shows the propagation of the excitation on the ladder schematically (top) and as measured in the 1ES (bottom). Similarly to the AB ring above, the evolution exhibits TRSB and is determined by the local fluxes through the ladder's plaquettes. The excitation hops to site 3, then splits to sites 1 and 4, and finally recombines back at site 2, that is, following the depicted green current arrows. We note that, due to symmetry $U_{1,4}$, the occupation of sites 1 and 4 can be in only a symmetric triplet state $|T_1\rangle = |T\rangle_{1,4}|00\rangle_{2,3}$, excluding $|S_1\rangle$ from the dynamics.

Next, we initialize the system to site $|1\rangle$ as shown in Fig. 5(b). Similarly to above, TRSB is manifested in the spin-excitation trajectory. We observe the peak occupation encompassing the ladder in a counterclockwise manner, following the path $1 \to 2 \to 4 \to 3 \to 1$. Here, the initial state is an equal superposition of $|S_1\rangle$ and $|T_1\rangle$; hence, the occupation of site 4 is a result of an accumulation of a phase difference between these states. The spin-current patterns demonstrated here are in agreement with Ref. [67], for the frustration-free regime. We compare the dynamics shown in Figs. 5(a) and 5(b) to a numerical evaluation of the evolution, with Ω given by a ML fit, yielding $\Omega = 245 \pm 2$ Hz with 95% probability.

We now turn to the 2ES. Here, the four-body correlated hop term, shown in Eq. (5), becomes active and modifies the system's evolution. A similar symmetry-based analysis reveals that the 2ES spectrum is composed of the energies 0, $\pm\Omega$, and $\pm E_2$, with E_2 evaluated by direct diagonalization as 3Ω. We conclude that the 2ES evolution as well is periodic with period $T_{2\mathrm{ES}} = 2\pi/\Omega$. The difference between E_1 and E_2 is a clear signature of interactions; i.e., the four-body interaction in Eq. (5) modifies the 2ES spectrum [when removing the four-body term from Eq. (5), the spectrum is $\pm E_1, 0$ for all eigenstates].

We initialize the system to the state $|1,2\rangle$, with $|i,j\rangle = \sigma_i^+\sigma_j^+|0000\rangle$, as shown in Fig. 6(a). This initial state evolution is directly affected by the four-body term $\psi_1\psi_3^\dagger n_2$; i.e., the presence of an excitation on site 2 modifies the hop $1 \to 3$. Indeed, we observe modified dynamics with respect to the separate evolution of these two excitations in the 1ES. Specifically, the state evolves to $|1,3\rangle$, as opposed to the 1ES evolution $|1\rangle \to |2\rangle$ in Figs. 5(a) and 5(b). Similarly, the state then evolves to $|2,4\rangle$ as opposed to the 1ES evolution $|3\rangle \to |1\rangle$.

Next, we initialize the system in the state $|1,4\rangle$, which is a $+1$ eigenstate of $U_{1,4}$, shown in Fig. 6(b). The initial state occupies only $E=0$ and $E=\pm 3\Omega$ states; thus, the evolution is periodic with period $T_{2ES}/3 = 2\pi/3\Omega$, which is observed in the data. We compare the dynamics shown in Figs. 6(a) and 6(b) to a numerical evaluation of the evolution, with Ω given by a ML fit, yielding $\Omega = 246 \pm 2$ Hz with 95% probability, in complete agreement with the 1ES data, confirming the theoretical modeling of the system, including the interactions between excitations in the 2ES.

IV. CONCLUSIONS

Our measurements, shown above, constitute a first demonstration of quantum simulations of TRSB systems in a trapped-ion quantum computer, enabled by the methods detailed in Refs. [41,42]. We observe the complex dynamics generated by the combination of programmable strong interactions and TRSB. The flexibility and scalability of our methods will enable future exploration of more complex models, measuring both nonequilibrium and ground-state properties of a variety of coupling geometries. The embedding of the simulator in a programmable quantum computer can be leveraged to certify ground states, as shown, but also to measure complex observables, including high-order correlations needed to probe topological order parameters; measure nonlinear observables such as entanglement entropy through the use of randomized measurements; and the use of hybrid quantum-classical optimization to probe ground states of complex spin systems. By conservatively improving our experimental setup, our method can be scaled up to study more complicated models for longer evolution times. Specifically, the same methods used here can be easily generalized to simulate longer AB rings and triangular ladders, as well as more complicated structures such as helices, tori, and Möbius strips, threaded by magnetic fluxes. A small addition to the system, such as local control of the ions, will enable implementation of square lattices, disordered systems, and adiabatic ground-state preparation of multiple excited subspaces.

ACKNOWLEDGMENTS

We thank Rotem Arnon-Friedman, Anna Keselman, Meirav Pinkas, Boaz Raz, and Hagai Edri for helpful discussions. This work was supported by the Israel Science Foundation, the Israel Science Foundation—Quantum program, the Israeli Ministry of Science Technology and Space, and the Minerva Stiftung.

APPENDIX A: DEPHASING ESTIMATION OF QUENCH DYNAMICS

As shown in the main text, our excitation dynamics data exhibit dephasing which is not present in the Aharonov-Bohm or triangular ladder Hamiltonians. This is despite the fact that the evolution is normalized to the 1ES which is a DFS and that our state preparation and measurement error are typically above 95%.

Here, we show that this dephasing effect is due to a buildup of incoherent population in states outside of the DFS, which are nevertheless utilized to mediate the interactions within the DFS. We model this buildup and show it captures the measured subspace occupation data, as well as the dephasing within the DFS. Furthermore, this dephasing mechanism delineates the route to scaling up our method, without suffering from increased dephasing, which is by conservatively increasing the single-qubit coherence time and drive power, compared to this work.

We start by estimating the population buildup outside of the DFS. As described in Ref. [42], the coupling of an nth NN hopping term, H_n, in Eq. (1) is proportional to $\eta^2\Omega^2/\xi$, with η the Lamb-Dicke parameter associated with the center-of-mass mode of motion of the ion chain, Ω the carrier Rabi frequency, and ξ a detuning of the laser drive from the motional sideband. To generate fast enough dynamics such that the essential physical properties are observed requires a large laser Rabi frequency or small detuning ξ.

However, a small ξ generates non-negligible population in unwanted states. For example, we initialize the state $|100\rangle$ of the 1ES in Fig. 2(a) and observe a "hop" to the state $|010\rangle$, which is, in fact, mediated by populating the connecting state, $|110\rangle$, of the 2ES, at intermediate times. We estimate the population in these subspaces by first taking one state in the 1ES, e.g., $|100\rangle$, and one state in the 2ES, e.g., $|110\rangle$, which are coupled by the Hamiltonian:

$$H_{1\leftrightarrow 2} = \frac{\xi}{2}\tau_z + \frac{\eta\Omega}{2}\tau_x, \tag{A1}$$

with τ_i Pauli operators connecting the two states. Furthermore, the two states experience dephasing, as they do not occupy the same DFS. Thus, we use a Lindblad jump operator and model this dynamics as

$$\partial_t\rho = -i[H_{1\leftrightarrow 2},\rho] + \frac{\gamma_2}{2}\mathcal{L}[\tau_z](\rho), \tag{A2}$$

with ρ the density operator describing the two states, γ_2^{-1} the single-qubit coherence time, and the Lindblad superoperator $\mathcal{L}[O](\rho) = O\rho O^\dagger - \{\rho, O^\dagger O\}/2$, with the jump operator O used for dephasing is τ_z.

In the limit $\xi \gg \eta\Omega, \gamma_2$, which is maintained in our implementation, Eq. (A2) can be solved showing that the population of an initially unoccupied state in the 2ES is given by

$$P_{2ES} = \frac{1}{2} - \frac{1}{2}e^{-\gamma_{\text{eff}}t}, \tag{A3}$$

with an effective decay rate $\gamma_{\text{eff}} = (\eta^2\Omega^2/\xi^2)\gamma_2$. In this trivial model, $P_{1ES} = P_{DFS} = 1 - P_{2ES}$. This result is

intuitive; in the absence of dephasing, the Hamiltonian generates off-resonance Rabi oscillations, which in the limit above corresponds to an oscillation of the population in the 2ES at rate ξ and amplitude $\eta^2\Omega^2/\xi^2$. The dephasing gradually decoheres these oscillations, which leads to a buildup of population at a rate corresponding to the single-qubit coherence time, scaled by the oscillation's amplitude.

The spin models we implement in this work are generated by driving several tones, detuned by ξ_m from the motional sidebands and with corresponding power Ω_m, with $m = 1, \ldots, 8$ (see below). Furthermore, other subspaces such as the 0ES are also similarly coupled during the system's evolution. Therefore, we generalize our argument by modifying the effective decay rate:

$$\gamma_{\text{eff}} \to N\gamma_2 \sum_n (\eta\Omega_n/\xi_n)^2, \tag{A4}$$

with N the number of ions. We use this to estimate the population in the subspace we initialized to:

$$P_{\text{DFS}} = \frac{1}{2} + \frac{1}{2} e^{-\gamma_{\text{eff}} t}. \tag{A5}$$

In our implementations, we independently evaluate $\gamma_2^{-1} = 1.19 \pm 0.03$ ms using standard Ramsey measurements. Together with the drive's spectral information (see below), we are able to predict the population in the initialized subspaces. These generate good estimation, without fitting, of the observed subspace occupation, as seen in Figs. 7 and 9 (dashed black line, below).

Next, we show that the buildup of incoherent population acts as a mediator of dephasing within the DFS. Because our data are postselected on the correct occupation subspace, i.e., the subspace we initialized to (see below), the dephasing is quadratic in time and not linear, allowing observation of longer coherent dynamics.

As an example, we take the AB Hamiltonian in Eq. (3), in the 1ES, with $\Phi_{\text{AB}} = 0$ and $N = 3$. That is, the Hamiltonian

$$H_{\text{AB}} = \Omega \begin{pmatrix} 0 & 1 & 1 \\ 1 & 0 & 1 \\ 1 & 1 & 0 \end{pmatrix}. \tag{A6}$$

We model the mediation of coupling in a Lindbladian equation:

$$\begin{aligned} \partial_t \rho &= -i[H_{\text{AB}}, \rho] + \frac{\gamma_2}{2}[1 - P_{\text{DFS}}(t)] \sum_{n=1}^{3} \mathcal{L}[|n\rangle\langle n|](\rho) \\ &\equiv \mathcal{D}_t(\rho); \end{aligned} \tag{A7}$$

that is, the state evolves according to the coherent AB Hamiltonian but dephases according to the single-qubit dephasing rate γ_2, which is normalized by the population outside of the 1ES. The Lindblad jump operator $\mathcal{L}[|n\rangle\langle n|](\rho)$ simply causes a dephasing of the nth site in the AB ring. The second row in Eq. (A7) defines the linear operation acting on ρ using the time-dependent superoperator, $\mathcal{D}_t$.

Equation (A7) constitutes a time-dependent ordinary differential equation. However, since $\gamma_{\text{eff}} \ll \Omega$, it can be solved by assuming adiabatic following. That is, we estimate the resulting population dynamics by considering the evolution of a fully coherent model and rescaling it according to a decaying envelope $E_{\text{DFS}}(t)$, such that $p_n(t) \to E_{\text{DFS}}(t)p_n(t) + (1/N_{\text{DFS}})[1 - E_{\text{DFS}}(t)]$, with $p_n(t)$ the population of site n due to only Hamiltonian evolution and N_{DFS} the number of states in the DFS.

Specifically, we estimate E_{DFS} by considering the eigenvalues and eigenstates of the instantaneous $\mathcal{D}_t$. Its diagonalization reveals that the decay in the system is given by the eigenvalue

$$\lambda(t) = -\frac{\gamma_2}{4}(e^{-\gamma_{\text{eff}} t} - 1). \tag{A8}$$

Therefore, we estimate

$$\begin{aligned} E_{\text{DFS}}(t) &= \exp\left(\int_0^t dt' \lambda(t')\right) \\ &= \exp\left(-\frac{\gamma_2}{4\gamma_{\text{eff}}}(e^{-\gamma_{\text{eff}} t} - 1 + \gamma_{\text{eff}} t)\right). \end{aligned} \tag{A9}$$

We note that in leading order the envelope is $E_{\text{DFS}}(t) = \exp(-\frac{1}{8}\gamma_2\gamma_{\text{eff}} t^2)$, with corrections in higher orders of $\gamma_{\text{eff}} t$. Thus the buildup of incoherent population outside of the DFS "leaks" into the DFS as dephasing. However, due to our use of postselection, the decay is quadratic in short times, leading to an initially slow decay, i.e., slower than the loss of population from the subspace.

We use $E_{\text{DFS}}(t)$ in order to rescale the population dynamics predicted by the Hamiltonian evolution of our simulated models (using similar considerations for the triangular ladder model). As seen in the solid lines in Figs. 2, 5, and 6, these estimations generate a good prediction of the observed dynamics, without fitting the decay parameters.

Figure 8 below shows the effect of both population leakage out of the DFS and dephasing within the DFS (dashed black line) on unprocessed data, i.e., data with no postselection.

This analysis also indicates what is necessary in order to efficiently scale up the simulated models while ensuring a high-fidelity simulation. Decoherence effects can be mitigated by improving the system coherence times such that small populations outside of the decoherence-free subspace will not cause significant decoherence. For example, using

a magnetic field shielding or qubits based on clock states show long coherence times in numerous trapped-ion systems. Clearly, such a solution cannot be implemented together with the application of an external magnetic field gradient; however, a qubit transition frequency difference can be generated with alternative methods, e.g., by using an additional shaped laser beam that generates an appropriate light shift profile on the ion chain. In addition, increasing the laser power, together with increasing ξ, acts to reduce the population in the intermediate states, thus avoiding the effects of decoherence altogether.

For example, increasing the single-qubit coherence time to 100 ms (100-fold increase compared to this work) and increasing the laser power to 100 mW (tenfold increase compared to this work), which are both conservative changes to our setup, allows one to simulate dynamics which decay out of the subspace 100 times slower and evolve 10 times faster than this work.

APPENDIX B: ADDITIONAL DYNAMICS MEASUREMENT DETAILS

As mentioned in the main text, our setup measures the σ_z operator at each site independently [41] (other Pauli operator measurements are performed by rotating the state prior to the σ_z measurement). Thus, after repeating the same experiment several times, we reconstruct a probability distribution over all 2^n states (but not the phase relation between them). We use this information in order to postselect and renormalize the results shown in Figs. 2, 5, and 6 to the relevant excitation subspace. For example, Fig. 2(a) shows an initial single excitation in a three-site model; thus, the data shown for the occupation of site number 1 (blue) are transformed as $\Pr(|100\rangle) \mapsto \Pr(|100\rangle)/[\Pr(|100\rangle) + \Pr(|010\rangle) + \Pr(|001\rangle)]$, with $\Pr(|n_1 n_2 n_3\rangle)$ the measured probability of observing the state $|n_1 n_2 n_3\rangle$ and $n_i \in 0, 1$. This means that, in this dataset, measurements yielding 0, 2, or 3 excitations are ignored.

We present the evolution of the occupation of the different subspaces corresponding to the data in the main text. Figure 7 shows the occupation of the different subspaces in the AB ring model, corresponding to Fig. 2. We note that the 1ES occupation in Figs. 7(a)–7(c) and 2ES occupation in Fig. 7(d) decays but remains larger than 0.5 throughout the evolution. We also add the expected population in the DFS according to the prediction of Eq. (A5).

We present examples of unprocessed data, i.e., without subspace normalization. Figure 8 shows the full occupation data in the AB ring dynamics experiments, with Fig. 8(a) corresponding to Figs. 2(a) and 8(b) corresponding to Fig. 2(d). The main features discussed in the main text are clearly observed in this dataset, as well as negligible population in the other subspaces. Furthermore, our prediction for the decay, given by Eqs. (A5) and (A9), shows a good fit to the measured data.

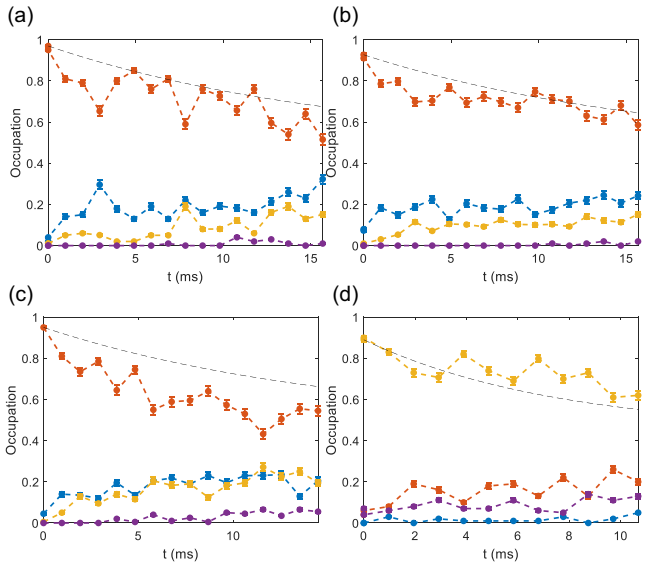

FIG. 7. Subspace occupancy of AB ring experiments. With zero (blue), one (red), two (orange), and three (purple) excitations present. (a)–(d) correspond to Figs. 2(a)–(d), respectively. The dashed black line shows the expected population in the DFS, according to Eq. (A5). The initial estimate is scaled by the preparation fidelity, i.e., the first data point. Error bars represent standard deviation due to quantum shot noise.

Figure 9 shows the subspace occupation in the triangular ladder, corresponding to Figs. 5 and 6. We also add the predicted population in the DFS according to the estimate in Eq. (A5).

The magnetic gradient generated on the ion chain is measured using correlation spectroscopy in a Ramsey-like experiment. A similar protocol is used in Ref. [68]. Specifically, all ions are prepared in the $|0\rangle$ state and are then rotated to the $|+\rangle = (|0\rangle + |1\rangle)/\sqrt{2}$ state using a global $\pi/2$ pulse. The ions then freely evolve under the influence of the magnetic gradient for some time t, after

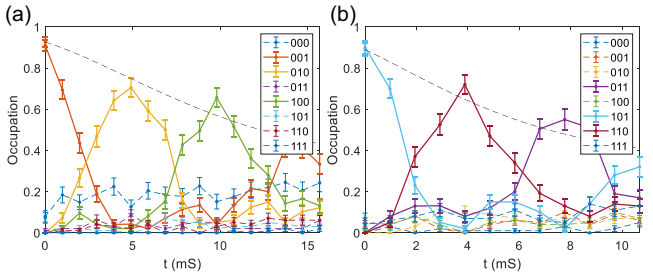

FIG. 8. Unprocessed data of the AB ring dynamics. States in the initialized excitation subspace (bold lines) are primarily excited, while other states (dashed lines) have negligible populations. (a) Corresponding to Fig. 2(a). (b) Corresponding to Fig. 2(d). The dashed black line shows the expected population decay according to Eqs. (A5) and (A9), scaled by the initial preparation fidelity, i.e., by the first data point. Error bars represent standard deviation due to quantum shot noise.

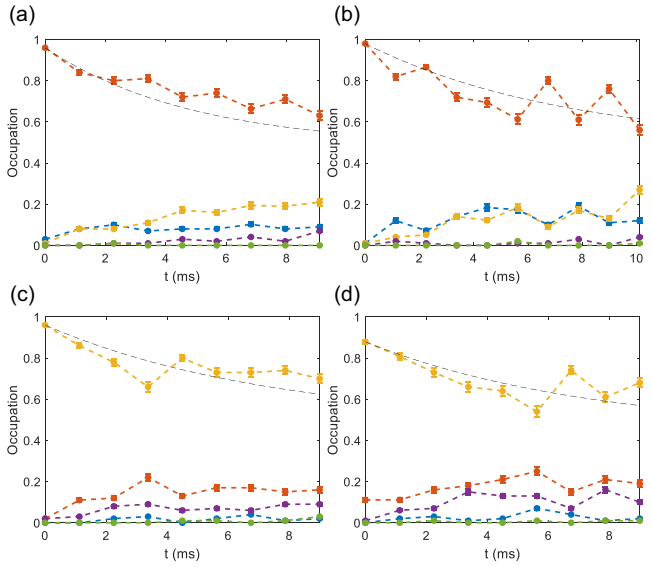

FIG. 9. Subspace occupancy of triangular ladder ring experiments with zero (blue), one (red), two (orange), three (purple), and four (green) excitations present. (a) and (b) correspond to Figs. 5(a) and 5(b), respectively. (c) and (d) correspond to Figs. 6(a) and 6(b), respectively. The dashed black line shows the expected population in the DFS, according to Eq. (A5). The initial estimate is scaled by the preparation fidelity, i.e., the first data point. Error bars represent standard deviation due to quantum shot noise.

which they are rotated using an additional $\pi/2$ pulse. We then measure the individual σ_z component and compute the parity signal of adjacent ions, i.e., the number $P = \Pr(|00\rangle) + \Pr(|11\rangle) - \Pr(|10\rangle) - \Pr(|01\rangle)$, which oscillates at the relative transition frequency difference of the two ions, i.e., in the frequency Δ generated by the gradient.

Figure 10 shows typical measurements (markers with dashed lines) and the corresponding fitted parity

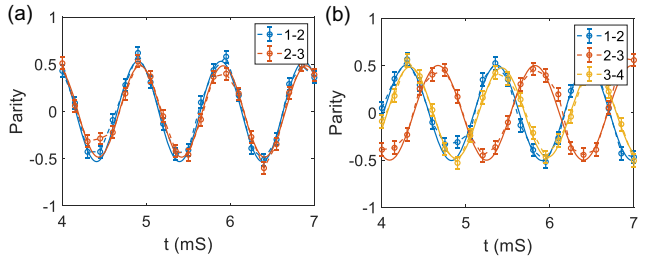

FIG. 10. Parity measurement used to determine the frequency difference between adjacent ions, for three ions (a) and four ions (b). The data (points connected by a dashed line) show parity oscillations between adjacent ions (see the legend) and are fitted (solid line) in order to determine the frequency difference. Error bars represent standard deviation due to quantum shot noise. As seen for four ions, the frequency difference between ions 2 and 3 is different than the rest due to unequal spacing of the ion chain.

oscillations (solid lines) used to obtain Δ for three ions (a), for which we estimate $\Delta = 1012 \pm 31$ Hz, and four ions (b). In our trap, the ions are not positioned at equal distances from each other; thus, they exhibit various differential frequencies, and we obtain $\Delta_{1,2} = \Delta_{3,4} = 922 \pm 35$ Hz and $\Delta_{3,4} = 866 \pm 35$ Hz, with $\Delta_{i,j}$ the transition frequency difference between ions i and j. Clearly, a trap which uses anharmonic potentials to generate equally spaced ions or a programmable method of generating a constant energy difference along the ion chain, e.g., tunable light shift, can mitigate these effects.

Using the measured values of Δ and values such as the carrier Rabi frequency and the center-of-mass sideband frequency (measured in standard methods), we generate the spectral tones required to implement our models. In principle, each H_n term in Eq. (1) requires two tones. However, in this work, we use four tones per H_n term, as we show in Ref. [41] that the additional terms act to mitigate unwanted effects, e.g., inhomogeneous broadening. In general, we use the frequencies

$$\omega^b_{n,\pm} = \omega_0 + \delta + (\nu + \xi_n) \pm n\Delta/2, \tag{B1}$$

$$\omega^r_{n,\pm} = \omega_0 + \delta - (\nu + \xi_n) \pm n\Delta/2, \tag{B2}$$

with $\omega^b_{n,\pm}$ ($\omega^r_{n,\pm}$) a frequency pair addressing the blue (red) sideband, ω_0 the single-qubit transition frequency, Δ the frequency difference per ion as discussed above, ν the frequency of the center-of-mass mode of motion, ξ a "symmetric" detuning, and δ an "asymmetric" detuning from the two-photon transition.

As discussed in detail in Ref. [42], at low values of ξ unwanted nonresonant Hamiltonian terms can affect the simulation fidelity (in addition to decoherence discussed above); however, large values of ξ result in slower dynamics. These considerations are encapsulated in the dimensionless number $\beta = \xi/2\Omega_n = \xi\Delta/(\eta\Omega)^2$, with η the Lamb-Dicke parameter associated with the motional mode and Ω the carrier Rabi frequency. The role of δ is to suppress transitions of the form $\sigma^+\sigma^+$ and $\sigma^-\sigma^-$, which are associated with a resonant absorption of one $\omega^r_{n,\pm}$ photon and one $\omega^b_{n,\pm}$ photon.

For the generation of the quench dynamics shown in Fig. 2, we use H_1 and H_2 (and all else zero). To this end, we use $\beta \approx 6$, $\nu \approx 1$ MHz, and $\Omega \approx 60$ kHz, yielding $\xi_1 = 28.1$ kHz. Furthermore, we choose $\delta = \xi_1/2$.

As shown in Eq. (B2), the value of ξ depends on n; this is done in order to avoid unwanted resonances. We choose $\xi_2 = 1.25\xi_1 = 35.1$ kHz. Since we are interested in equal coupling strengths of all the links in the ring, we compensate the difference in symmetric detuning using the power; thus, we drive the ω_2's at a relative power $r_2/r_1 = \sqrt{\xi_2/\xi_1}$. In order to observe time-reversal-breaking dynamics, we set the phase of the different tones to $\phi_{n,\pm} = \pm\Phi/6$, with Φ

the flux penetrating the ring and in correspondence to the notation in Eq. (B2).

APPENDIX C: ERROR BAR ESTIMATIONS

All of the error bars shown in the main text and below correspond to $\pm 1\sigma$ estimations due to quantum shot noise. These errors are propagated using standard methods, i.e., $\delta f(\boldsymbol{x}) = \sqrt{\sum_i (\partial_{x_i} f \cdot \delta x_i)^2}$, for computing error bars for postselected, renormalized data (see below), as well as for computing the energy, current, and overlap with the ground state, in the adiabatic ground-state preparation section. The error estimations for the dynamics data in Figs. 2, 5, and 6 are due to 100 repetitions of each evolution time. The error estimations for the ground-state preparation data are due to 200 repetitions per flux point.

APPENDIX D: ADIABATIC GROUND-STATE PREPARATION

In the main text, we state that we do not precisely implement the AB Hamiltonian $H_{\mathrm{AB}}(\Phi_{\mathrm{AB}})$ in Eq. (3). Rather, we implement the Hamiltonian $H_{\mathrm{eff}} = H_{\mathrm{AB}}(\Phi_{\mathrm{AB}}) + \epsilon H_{\mathrm{AB}}(0)$, such that the factor that accompanies a hop is modified: $e^{i\Phi_{\mathrm{AB}}} \to e^{i\Phi_{\mathrm{AB}}} + \epsilon$.

In our method, we use pairs of spectral tones to resonantly bridge the frequency gap Δ between adjacent ions, opened by the magnetic field gradient. However, a single tone may off-resonantly mediate a NN hop as well. Since the same beam is used to excite and deexcite the ions to mediate a hop, its phase is irrelevant, and it cannot carry a flux, i.e., $\Phi = 0$. We estimate the coupling of this effect by comparing the on-resonance coupling rate $\Omega_{n=1}$ and the detuning Δ in a two-photon Raman coupling, yielding the estimate $\Omega_{\Phi=0} = \Omega_{n=1}^2/\Delta$. In our implementation, we have $\Omega_{n=1} \approx 350$ Hz and $\Delta \approx 1$ kHz, yielding $\Omega_{\Phi=0}/\Omega_{n=1} \approx 0.35$.

In practice, we obtain the value of ϵ and Ω with a maximum likelihood fit. Specifically, we simulate an ideal adiabatic ramp of H_{AB} in the 1ES (i.e., a three-dimensional Hamiltonian) and choose the values of ϵ and Ω, such that they maximize the probability to measure our obtained data. We obtain $\epsilon = 0.22$ and $\Omega = 350$ Hz.

We note that due to the expression for Ω_n we have $\Omega_{\Phi=0}/\Omega_{n=1} \propto \Omega_0^2/\Delta^2$, with Ω_0 the carrier Rabi frequency. Thus, this effect can be mitigated by increasing Ω_0 and Δ such that Ω_n is unchanged but $\Omega_{\Phi=0}$ is suppressed.

In the main text, we state that tomography of the resulting prepared state is performed by occupancy and correlation measurements, under the assumption of rapid dephasing of other excitation subspaces. Indeed, assuming the prepared state $|\psi\rangle = \sqrt{p_1}e^{i\phi_1}|100\rangle + \sqrt{p_2}e^{i\phi_2}|010\rangle + \sqrt{p_3}e^{i\phi_3}|001\rangle$, then the occupancy measurement is equivalent to evaluating $\langle\sigma_z\rangle$ for each of the three sites. Similarly, evaluating $\langle\sigma_z^j\sigma_z^{j+1}\rangle$ after the in-phase measurement procedure yields $\frac{2}{3}p_j p_{j+1}\cos(\theta_j - \theta_{j+1})$ and after the out-of phase correlation procedure yields $\langle\sigma_z^1\sigma_z^2\rangle = \frac{2}{3}p_1 p_2 \sin(\theta_1 - \theta_2)$ and $\langle\sigma_z^2\sigma_z^3\rangle = \frac{2}{3}p_2 p_3 \sin(\theta_2 - \theta_3)$. These combined are enough to reconstruct $|\psi_f\rangle$ up to a global phase.

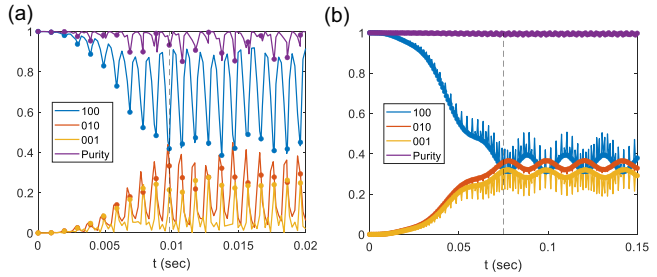

FIG. 11. Simulation of adiabatic ground-state preparation of the AB ring. (a) Preparation with parameters similar to the experiment, with $\Phi = \pi/2$ and $\beta = 7$. The adiabatic ramp starts at $t = 0$ and ends at $t = 10$ ms (dashed line). The resulting state occupies the three 1ES states almost equally at stroboscopic times (markers) and is coherent, as seen by the high purity values. (b) Preparation deep in the adiabatic regime with $\beta = 40$ and $\Phi = 0$, the system evolves smoothly at all times and results in a high overlap with the AB Hamiltonian ground state.

To supplement the data, we perform a numerical simulation of the full ion-chain Hamiltonian of the adiabatic ramp [i.e., a $2^3(n_{\max}+1)$-dimensional Hamiltonian, with $n_{\max} = 9$ the maximum phonon occupation number of the chain's center-of-mass normal mode of motion]. Figure 11(a) shows the evolution of the different 1ES states under the adiabatic ramp protocol with $\Phi = \pi/2$ and the remaining parameters similar to those of the experiment, such that $\beta = \xi/2\Omega_n = 7$ [42]. The ramp starts at $t = 0$ and ends at 10 ms (dashed line), after which the resulting state is coherent, seen from its high purity (purple line) and occupies almost equally the three 1ES states (blue, red, and yellow lines) at the stroboscopic times (markers), indicating an approximate ground state of the underlying AB Hamiltonian.

We also repeat this simulation deep in the adiabatic regime, with $\beta = 40$ and $\Phi = 0$, shown in Fig. 11(b). Here, the procedure yields an even higher overlap with the underlying ground state. Furthermore, the large β value results in much less oscillation, making the result viable at all evolution times.

APPENDIX E: TRIANGULAR MODEL ANALYSIS

We provide further details on the four-site triangular ladder. Specifically, we show that the three symmetries $U_{1,4}$, $A_{2,3}$, and C, described in the main text, allow one to easily recognize seven of the 16 eigenstates. Furthermore, this analysis immediately shows periodicity of the 1ES evolution and of a subspace of the 2ES. A summary of the eigenstates is given in Table I.

We start by noticing that the unoccupied state $|\downarrow\downarrow\rangle|\downarrow\downarrow\rangle$ and the fully occupied state $|\uparrow\uparrow\rangle|\uparrow\uparrow\rangle$ are trivially $E = 0$

TABLE I. Eigenstates of the four-site triangular ladder at $\Phi_S = \pi/2$, which are straightforward to obtain. Showing the state, energy, and excitation subspace of each eigenstate.

State	$\langle H \rangle$	nES
$\|\downarrow\downarrow\rangle\|\downarrow\downarrow\rangle$	0	0
$\|\uparrow\uparrow\rangle\|\uparrow\uparrow\rangle$	0	4
$\|S\rangle\|\downarrow\downarrow\rangle$	0	1
$\|S\rangle\|\uparrow\uparrow\rangle$	0	3
$\|S\rangle\frac{\|\uparrow\downarrow\rangle - i\|\downarrow\uparrow\rangle}{\sqrt{2}}$	Ω	2
$\|S\rangle\frac{\|\uparrow\downarrow\rangle + i\|\downarrow\uparrow\rangle}{\sqrt{2}}$	$-\Omega$	2
$\frac{\|\uparrow\uparrow\rangle\|\downarrow\downarrow\rangle - \|\downarrow\downarrow\rangle\|\uparrow\uparrow\rangle}{\sqrt{2}}$	0	2

eigenstates of the system, as all Hamiltonian terms annihilate them. Here and in all other states below, the two kets are to be understood as $|\psi\rangle|\varphi\rangle \equiv |\psi\rangle_{1,4}|\varphi\rangle_{2,3}$.

Next, because of $U_{1,4}$, when sites 1 and 4 form a spin singlet, they are decoupled from the evolution. Therefore, a set of eigenstates can be found by diagonalizing the remaining terms connecting sites 2 and 3. In the 1ES, this comes about as $|S\rangle|\downarrow\downarrow\rangle$, with $E = 0$. The chiral symmetry now forces the three remaining eigenstates of the 1ES to have energies $0, \pm E_1$, with E_1 determined by exact diagonalization of the 3×3 Hamiltonian. Similarly, in the 3ES, we have $|S\rangle|\uparrow\uparrow\rangle$, with $E = 0$.

In the 2ES, a singlet on sites 1 and 4 requires an additional excitation on sites 2 and 3. The interaction between these sites takes the form of a σ_y term; thus, two eigenstates in the 2ES are $|S\rangle(|\uparrow\downarrow\rangle \pm i|\downarrow\uparrow\rangle/\sqrt{2})$ with energy $\mp\,\Omega$. The state $(|\uparrow\uparrow\rangle|\downarrow\downarrow\rangle - |\downarrow\downarrow\rangle|\uparrow\uparrow\rangle/\sqrt{2})$ is an additional eigenstate in the 2ES, carrying 0 energy. Similarly to above, the remaining three states must carry energies $0, \pm E_2$, with E_2 determined by exact diagonalization.

[1] B. I. Halperin, *Statistics of Quasiparticles and the Hierarchy of Fractional Quantized Hall States*, Phys. Rev. Lett. **52**, 1583 (1984).

[2] D. Arovas, J. R. Schrieffer, and F. Wilczek, *Fractional Statistics and the Quantum Hall Effect*, Phys. Rev. Lett. **53**, 722 (1984).

[3] B. I. Halperin and J. K. Jain, *Fractional Quantum Hall Effects: New Developments* (World Scientific, Singapore, 2020).

[4] H. Bartolomei, M. Kumar, R. Bisognin, A. Marguerite, J.-M. Berroir, E. Bocquillon, B. Plaçais, A. Cavanna, Q. Dong, U. Gennser, Y. Jin, and G. Fève, *Fractional Statistics in Anyon Collisions*, Science **368**, 173 (2020).

[5] J. Nakamura, S. Liang, G. C. Gardner, and M. J. Manfra, *Direct Observation of Anyonic Braiding Statistics*, Nat. Phys. **16**, 931 (2020).

[6] C. Monroe, W. C. Campbell, L.-M. Duan, Z.-X. Gong, A. V. Gorshkov, P. W. Hess, R. Islam, K. Kim, N. M. Linke, G. Pagano, P. Richerme, C. Senko, and N. Y. Yao, *Programmable Quantum Simulations of Spin Systems with Trapped Ions*, Rev. Mod. Phys. **93**, 025001 (2021).

[7] E. Altman *et al.*, *Quantum Simulators: Architectures and Opportunities*, PRX Quantum **2**, 017003 (2021).

[8] N. Cooper, *Fractional Quantum Hall States of Bosons: Properties and Prospects for Experimental Realization*, in *Fractional Quantum Hall Effects: New Developments* (World Scientific, Singapore, 2020), pp. 487–521.

[9] M. Aidelsburger, S. Nascimbene, and N. Goldman, *Artificial Gauge Fields in Materials and Engineered Systems*, C. R. Phys. **19**, 394 (2018).

[10] D. Jaksch and P. Zoller, *Creation of Effective Magnetic Fields in Optical Lattices: The Hofstadter Butterfly for Cold Neutral Atoms*, New J. Phys. **5**, 56 (2003).

[11] Y.-J. Lin, R. L. Compton, K. Jiménez-García, J. V. Porto, and I. B. Spielman, *Synthetic Magnetic Fields for Ultracold Neutral Atoms*, Nature (London) **462**, 628 (2009).

[12] Y.-J. Lin, K. Jiménez-García, and I. B. Spielman, *Spin-Orbit-Coupled Bose-Einstein Condensates*, Nature (London) **471**, 83 (2011).

[13] J. Dalibard, F. Gerbier, G. Juzeliūnas, and P. Öhberg, *Colloquium: Artificial Gauge Potentials for Neutral Atoms*, Rev. Mod. Phys. **83**, 1523 (2011).

[14] I. Bloch, J. Dalibard, and S. Nascimbene, *Quantum Simulations with Ultracold Quantum Gases*, Nat. Phys. **8**, 267 (2012).

[15] J. Struck, M. Weinberg, C. Ölschläger, P. Windpassinger, J. Simonet, K. Sengstock, R. Höppner, P. Hauke, A. Eckardt, M. Lewenstein, and L. Mathey, *Engineering Ising-XY Spin-Models in a Triangular Lattice Using Tunable Artificial Gauge Fields*, Nat. Phys. **9**, 738 (2013).

[16] M. Aidelsburger, M. Atala, M. Lohse, J. T. Barreiro, B. Paredes, and I. Bloch, *Realization of the Hofstadter Hamiltonian with Ultracold Atoms in Optical Lattices*, Phys. Rev. Lett. **111**, 185301 (2013).

[17] H. Miyake, G. A. Siviloglou, C. J. Kennedy, W. C. Burton, and W. Ketterle, *Realizing the Harper Hamiltonian with Laser-Assisted Tunneling in Optical Lattices*, Phys. Rev. Lett. **111**, 185302 (2013).

[18] M. Mancini, G. Pagano, G. Cappellini, L. Livi, M. Rider, J. Catani, C. Sias, P. Zoller, M. Inguscio, M. Dalmonte *et al.*, *Observation of Chiral Edge States with Neutral Fermions in Synthetic Hall Ribbons*, Science **349**, 1510 (2015).

[19] B. Stuhl, H.-I. Lu, L. Aycock, D. Genkina, and I. Spielman, *Visualizing Edge States with an Atomic Bose Gas in the Quantum Hall Regime*, Science **349**, 1514 (2015).

[20] N. R. Cooper, J. Dalibard, and I. B. Spielman, *Topological Bands for Ultracold Atoms*, Rev. Mod. Phys. **91**, 015005 (2019).

[21] A. Periwal, E. S. Cooper, P. Kunkel, J. F. Wienand, E. J. Davis, and M. Schleier-Smith, *Programmable Interactions and Emergent Geometry in an Array of Atom Clouds*, Nature (London) **600**, 630 (2021).

[22] P. Roushan, C. Neill, A. Megrant, Y. Chen, R. Babbush, R. Barends, B. Campbell, Z. Chen, B. Chiaro, A. Dunsworth *et al.*, *Chiral Ground-State Currents of Interacting Photons in a Synthetic Magnetic Field*, Nat. Phys. **13**, 146 (2017).

[23] C. Neill, T. McCourt, X. Mi, Z. Jiang, M. Niu, W. Mruczkiewicz, I. Aleiner, F. Arute, K. Arya, J. Atalaya

et al., *Accurately Computing the Electronic Properties of a Quantum Ring*, Nature (London) **594**, 508 (2021).

[24] V. Lienhard, P. Scholl, S. Weber, D. Barredo, S. de Léséleuc, R. Bai, N. Lang, M. Fleischhauer, H. P. Büchler, T. Lahaye, and A. Browaeys, *Realization of a Density-Dependent Peierls Phase in a Synthetic, Spin-Orbit Coupled Rydberg System*, Phys. Rev. X **10**, 021031 (2020).

[25] Y.-F. Wang, Z.-C. Gu, C.-D. Gong, and D. N. Sheng, *Fractional Quantum Hall Effect of Hard-Core Bosons in Topological Flat Bands*, Phys. Rev. Lett. **107**, 146803 (2011).

[26] B. Bauer, L. Cincio, B. P. Keller, M. Dolfi, G. Vidal, S. Trebst, and A. W. Ludwig, *Chiral Spin Liquid and Emergent Anyons in a Kagome Lattice Mott Insulator*, Nat. Commun. **5**, 1 (2014).

[27] G. Semeghini, H. Levine, A. Keesling, S. Ebadi, T. T. Wang, D. Bluvstein, R. Verresen, H. Pichler, M. Kalinowski, R. Samajdar, A. Omran, S. Sachdev, A. Vishwanath, M. Greiner, V. Vuletić, and M. D. Lukin, *Probing Topological Spin Liquids on a Programmable Quantum Simulator*, Science **374**, 1242 (2021).

[28] M. Cerezo, A. Arrasmith, R. Babbush, S. C. Benjamin, S. Endo, K. Fujii, J. R. McClean, K. Mitarai, X. Yuan, L. Cincio *et al.*, *Variational Quantum Algorithms*, Nat. Rev. Phys. **3**, 625 (2021).

[29] T. Brydges, A. Elben, P. Jurcevic, B. Vermersch, C. Maier, B. P. Lanyon, P. Zoller, R. Blatt, and C. F. Roos, *Probing Rényi Entanglement Entropy via Randomized Measurements*, Science **364**, 260 (2019).

[30] H.-Y. Huang, R. Kueng, and J. Preskill, *Predicting Many Properties of a Quantum System from Very Few Measurements*, Nat. Phys. **16**, 1050 (2020).

[31] D. Bluvstein, H. Levine, G. Semeghini, T. T. Wang, S. Ebadi, M. Kalinowski, A. Keesling, N. Maskara, H. Pichler, M. Greiner *et al.*, *A Quantum Processor Based on Coherent Transport of Entangled Atom Arrays*, Nature (London) **604**, 451 (2022).

[32] L. Postler, S. Heußen, I. Pogorelov, M. Rispler, T. Feldker, M. Meth, C. D. Marciniak, R. Stricker, M. Ringbauer, R. Blatt, P. Schindler, M. Müller, and T. Monz, *Demonstration of Fault-Tolerant Universal Quantum Gate Operations*, Nature (London) **605**, 675 (2022).

[33] J. M. Pino, J. M. Dreiling, C. Figgatt, J. P. Gaebler, S. A. Moses, M. Allman, C. Baldwin, M. Foss-Feig, D. Hayes, K. Mayer *et al.*, *Demonstration of the Trapped-Ion Quantum CCD Computer Architecture*, Nature (London) **592**, 209 (2021).

[34] L. Egan, D. M. Debroy, C. Noel, A. Risinger, D. Zhu, D. Biswas, M. Newman, M. Li, K. R. Brown, M. Cetina *et al.*, *Fault-Tolerant Control of an Error-Corrected Qubit*, Nature (London) **598**, 281 (2021).

[35] A. Sørensen and K. Mølmer, *Entanglement and Quantum Computation with Ions in Thermal Motion*, Phys. Rev. A **62**, 022311 (2000).

[36] C. Kokail, C. Maier, R. van Bijnen, T. Brydges, M. K. Joshi, P. Jurcevic, C. A. Muschik, P. Silvi, R. Blatt, C. F. Roos *et al.*, *Self-Verifying Variational Quantum Simulation of Lattice Models*, Nature (London) **569**, 355 (2019).

[37] M. K. Joshi, F. Kranzl, A. Schuckert, I. Lovas, C. Maier, R. Blatt, M. Knap, and C. F. Roos, *Observing Emergent Hydrodynamics in a Long-Range Quantum Magnet*, Science **376**, 720 (2022).

[38] W. L. Tan, P. Becker, F. Liu, G. Pagano, K. S. Collins, A. De, L. Feng, H. B. Kaplan, A. Kyprianidis, R. Lundgren, W. Morong, S. Whitsitt, A. V. Gorshkov, and C. Monroe, *Domain-Wall Confinement and Dynamics in a Quantum Simulator*, Nat. Phys. **17**, 742 (2021).

[39] A. Kyprianidis, F. Machado, W. Morong, P. Becker, K. S. Collins, D. V. Else, L. Feng, P. W. Hess, C. Nayak, G. Pagano *et al.*, *Observation of a Prethermal Discrete Time Crystal*, Science **372**, 1192 (2021).

[40] M. Qiao, Z. Cai, Y. Wang, B. Du, N. Jin, W. Chen, P. Wang, C. Luan, E. Gao, X. Sun, H. Tian, J. Zhang, and K. Kim, *Observing Frustrated Quantum Magnetism in Two-Dimensional Ion Crystals*, arXiv:2204.07283.

[41] T. Manovitz, Y. Shapira, L. Gazit, N. Akerman, and R. Ozeri, *Trapped-Ion Quantum Computer with Robust Entangling Gates and Quantum Coherent Feedback*, PRX Quantum **3**, 010347 (2022).

[42] T. Manovitz, Y. Shapira, N. Akerman, A. Stern, and R. Ozeri, *Quantum Simulations with Complex Geometries and Synthetic Gauge Fields in a Trapped Ion Chain*, PRX Quantum **1**, 020303 (2020).

[43] D. Hangleiter, M. Kliesch, M. Schwarz, and J. Eisert, *Direct Certification of a Class of Quantum Simulations*, Quantum Sci. Technol. **2**, 015004 (2017).

[44] H. C. Po, H. Watanabe, and A. Vishwanath, *Fragile Topology and Wannier Obstructions*, Phys. Rev. Lett. **121**, 126402 (2018).

[45] A. M. Turner, E. Berg, and A. Stern, *Gapping Fragile Topological Bands by Interactions*, Phys. Rev. Lett. **128**, 056801 (2022).

[46] D.-W. Wang, C. Song, W. Feng, H. Cai, D. Xu, H. Deng, H. Li, D. Zheng, X. Zhu, H. Wang, S.-Y. Zhu, and M. O. Scully, *Synthesis of Antisymmetric Spin Exchange Interaction and Chiral Spin Clusters in Superconducting Circuits*, Nat. Phys. **15**, 382 (2019).

[47] L. Peleg, N. Akerman, T. Manovitz, M. Alon, and R. Ozeri, *Phase Stability Transfer across the Optical Domain Using a Commercial Optical Frequency Comb System*, arXiv:1905.05065.

[48] R. Shankar, *Exact Solution of the Two-Dimensional Ising Model*, in *Quantum Field Theory and Condensed Matter: An Introduction* (Cambridge University Press, Cambridge, England, 2017), pp. 114–142.

[49] R. Shaniv, T. Manovitz, Y. Shapira, N. Akerman, and R. Ozeri, *Toward Heisenberg-Limited Rabi Spectroscopy*, Phys. Rev. Lett. **120**, 243603 (2018).

[50] Y. I. M. Büttiker and R. Landauer, *Josephson Behavior in Small Normal One-Dimensional Rings*, Phys. Lett. A **96**, 365 (1983).

[51] H.-F. Cheung, Y. Gefen, E. K. Riedel, and W.-H. Shih, *Persistent Currents in Small One-Dimensional Metal Rings*, Phys. Rev. B **37**, 6050 (1988).

[52] Y. Aharonov and D. Bohm, *Significance of Electromagnetic Potentials in the Quantum Theory*, Phys. Rev. **115**, 485 (1959).

[53] S. Viefers, P. Koskinen, P. S. Deo, and M. Manninen, *Quantum Rings for Beginners: Energy Spectra and Persistent Currents*, Physica (Amsterdam) **21E**, 1 (2004).

[54] B. A. Z. António, A. A. Lopes, and R. G. Dias, *Transport through Quantum Rings*, Eur. J. Phys. **34**, 831 (2013).
[55] A. Noguchi, Y. Shikano, K. Toyoda, and S. Urabe, *Aharonov-Bohm Effect in the Tunnelling of a Quantum Rotor in a Linear Paul Trap*, Nat. Commun. **5**, 3868 (2014).
[56] C. A. Downing and D. Zueco, *Non-reciprocal Population Dynamics in a Quantum Trimer*, Proc. R. Soc. A **477**, 20210507 (2021).
[57] C. K. Majumdar and D. K. Ghosh, *On Next-Nearest-Neighbor Interaction in Linear Chain. I*, J. Math. Phys. (N.Y.) **10**, 1388 (1969).
[58] T. Hikihara, L. Kecke, T. Momoi, and A. Furusaki, *Vector Chiral and Multipolar Orders in the Spin-1/2 Frustrated Ferromagnetic Chain in Magnetic Field*, Phys. Rev. B **78**, 144404 (2008).
[59] L. Amico, R. Fazio, A. Osterloh, and V. Vedral, *Entanglement in Many-Body Systems*, Rev. Mod. Phys. **80**, 517 (2008).
[60] Y.-F. Wang, C.-D. Gong, and Z. D. Wang, *Tuning Kinetic Magnetism of Strongly Correlated Electrons via a Staggered Flux*, Phys. Rev. Lett. **100**, 037202 (2008).
[61] S. Furukawa, M. Sato, and S. Onoda, *Chiral Order and Electromagnetic Dynamics in One-Dimensional Multiferroic Cuprates*, Phys. Rev. Lett. **105**, 257205 (2010).
[62] S. Furukawa, M. Sato, S. Onoda, and A. Furusaki, *Ground-State Phase Diagram of a Spin-1/2 Frustrated Ferromagnetic XXZ Chain: Haldane Dimer Phase and Gapped/Gapless Chiral Phases*, Phys. Rev. B **86**, 094417 (2012).
[63] T. Mishra, R. V. Pai, S. Mukerjee, and A. Paramekanti, *Quantum Phases and Phase Transitions of Frustrated Hard-Core Bosons on a Triangular Ladder*, Phys. Rev. B **87**, 174504 (2013).
[64] T. Mishra, R. V. Pai, and S. Mukerjee, *Supersolid in a One-Dimensional Model of Hard-Core Bosons*, Phys. Rev. A **89**, 013615 (2014).
[65] E. Anisimovas, M. Račiūnas, C. Sträter, A. Eckardt, I. B. Spielman, and G. Juzeliūnas, *Semisynthetic Zigzag Optical Lattice for Ultracold Bosons*, Phys. Rev. A **94**, 063632 (2016).
[66] F. A. An, E. J. Meier, and B. Gadway, *Engineering a Flux-Dependent Mobility Edge in Disordered Zigzag Chains*, Phys. Rev. X **8**, 031045 (2018).
[67] J. Cabedo, J. Claramunt, J. Mompart, V. Ahufinger, and A. Celi, *Effective Triangular Ladders with Staggered Flux from Spin-Orbit Coupling in 1D Optical Lattices*, Eur. Phys. J. D **74**, 123 (2020).
[68] R. Shaniv, N. Akerman, T. Manovitz, Y. Shapira, and R. Ozeri, *Quadrupole Shift Cancellation Using Dynamic Decoupling*, Phys. Rev. Lett. **122**, 223204 (2019).